

Research Article

Effect of Intermediate Stiffeners on the Behaviors of Partially Concrete Encased Steel Beams

Cheng-Cheng Chen^{1,2} and Teguh Sudibyo^{1,3} 

¹Department of Civil and Construction Engineering, National Taiwan University of Science and Technology, Taipei 10607, Taiwan

²Taiwan Building Technology Center, National Taiwan University of Science and Technology, Taipei 10607, Taiwan

³Department of Civil Engineering, Universitas Gadjah Mada, Yogyakarta 55281, Indonesia

Correspondence should be addressed to Teguh Sudibyo; d10605809@mail.ntust.edu.tw

Received 16 March 2018; Revised 20 June 2018; Accepted 29 October 2018; Published 25 November 2018

Academic Editor: Melina Bosco

Copyright © 2018 Cheng-Cheng Chen and Teguh Sudibyo. This is an open access article distributed under the Creative Commons Attribution License, which permits unrestricted use, distribution, and reproduction in any medium, provided the original work is properly cited.

Partially concrete encased steel (PE) beams are composite steel beams and concrete elements that present several advantages, such as higher fire resistant, higher flexural capacity, and higher lateral torsional buckling resistant compared to bare steel beams. This paper reports an experimental study of eight PE beams under cyclic loading. The effectiveness of intermediate stiffeners, such as midspan stiffener and plastic hinge zone stiffener, in enhancing composite action and ductility of the PE beams was studied. The ductility performance of PE beams using strengthened beam-to-column connection and weakened beam-to-column connection was also investigated. The test results show that the plastic hinge zone stiffener performed well and has the potential to replace shear connectors. Strengthened and weakened beam-to-column connections can be implemented in PE beams to enhance the ductility of the PE beams; with the details of both strengthened and weakened beam-to-column connections determined by bare steel shape instead of the whole section. In addition, the suggestions to prevent premature failure of weakened beam-to-column connection were provide.

1. Introduction

Fire-proofing material is usually used to provide fire resistance to the steel members in high-rise buildings. The fire-proofing material may cause pollution to the environment; therefore, extra construction material is often needed to cover the fire-proofing material. Fully concrete encased steel beam or steel-reinforced concrete (SRC) beam, as shown in Figure 1(a), uses concrete to provide fire resistance to the steel in the beam; therefore, the pollution problem of fire proofing material can be avoided. However, the concrete brings extra vertical and seismic loads to the structure and the construction is comparatively more difficult and requires intensive labor.

The partially concrete encased steel beam shown in Figure 1(b) uses concrete in cooperation with fire-proofing coating to provide fire resistance to the steel beams. The concrete encasement on partially concrete encased beam can

effectively prevent the temperature of steel from rising sharply [2–4]. Compared to the SRC beams, this type of partially concrete encased steel beam, defined as PE beam hereafter, reduces the amount of concrete used, which reduces the vertical and seismic load on the structure. In addition, PE beams reduce the requirement for formwork, shoring, and steel cage fabrication. This reduces construction difficulties and cost. Furthermore, the presence of concrete infill between the steel flanges also contributes to PE beam to have higher bending resistance [5–8] and higher lateral-torsional buckling (LTB) resistance than bare steel beam [1, 9]. These advantages have led to wide application of PE beam to be used in modern construction. The PE beam shown in Figure 1(b) is the type of beam investigated here.

Several studies have been conducted to examine the composite action on PE beams. Kindmann et al. [5] investigated the composite behavior of PE beams under monotonic loading. It was found that shear connectors were

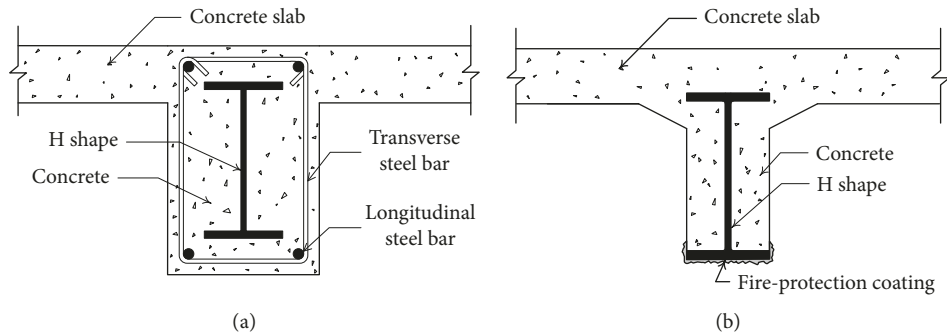


FIGURE 1: Concrete encased steel beam; adapted from “Behavior of Partially Concrete Encased Steel Beams under Cyclic Loading” [1]. (a) Fully concrete encased steel beam/SRC. (b) Partially concrete encased steel beam.

not necessary to develop composite action of the beams. However, the beams tested used tension reinforcement, which reduced the requirement for shear connectors. Nardin and Debs [6] examined the composite action of PE beams by testing simply supported rectangular beams with monotonic loading. The beam tested had enlarged bottom flange, which leads to higher requirement for shear connectors. Test results suggested that shear connectors are required for the beams to develop a composite action, and shear connectors installed on the bottom flange developed higher composite action than those installed on the web did. In addition, the slip between concrete and steel at the end of the test beams went beyond 2.0 mm at the time when the flexural strength was developed. Hegger and Goralski [7] evaluated the flexural capacity of PE beams which were integrated with concrete slab under both sagging and hogging moment. The test results showed that, when the beam under sagging moment, the flexural capacity of the beam with and without shear connection nearly had no difference. The load-deformation diagram of beam with and without shear connection could be recognized without any differences, with the load differences about 1%. The measured slip at the end of the concrete encasement was always less than 0.2 mm. The shear force was transferred by friction forces between the flanges of the steel profile and the concrete encasement. While under hogging moment, the beam without sufficient shear connection showed lower flexural strength. Chen et al. [8] conducted monotonic and cyclic tests on PE beams with span length of 0.75 m and 1.5 m (shear span ratio of 1.5 and 3, respectively). The plastic moment capacity is exceeded for all the test specimens and also showed good ductility under both monotonic and cyclic loading.

At present, research on PE beam used shear connection to develop the composite action between the steel shape and the concrete encasement which was tested by simply supporting with monotonic loading [5–7]. However, when a PE beam forms part of a moment resisting frame, as shown in Figure 2, the columns may provide constraint to the beam at the beam ends and suppress the slip between concrete and steel shape surfaces, as schematically explained in Figure 2(b). This column constraint should have positive effect on the development of beam composite action. However, when the distance between beam ends, or columns, is

too far, the effect of the column constraint may be reduced. In this case, extra stiffeners installed between the length of PE beam, referred as intermediate stiffeners, may provide extra constraint and further enhance the composite action. For the beam shown in Figure 2 subjected to earthquake type loading, a stiffener at the midspan, as shown in Figure 2(c), where bending moment changes direction, may be helpful. In addition, a stiffener installed near the plastic hinge zone, where the requirement for composite action is the highest in the beam span, should be advantageous to PE beam to develop its flexural strength.

In steel structures, it is common practice to move the plastic hinge away from the column surface to prevent premature fractures of the welds connecting the beam flange and the column flange. Strengthened beam-to-column connections (SBC) and weakened steel beam-to-column connections (WBC) have been suggested to solve this problem [10–14]. A PE beam has the same concerns as a steel beam has. And, it is of interest to the authors how PE beams perform when SBC or WBC is used.

In this study, a total of 8 PE beam specimens were fabricated and tested under cyclic loading. The effectiveness of column constraint and intermediate stiffeners, such as midspan stiffener and plastic hinge zone stiffener, was investigated. In addition, the suitability of SBC and WBC to PE beams is assessed.

2. Experimental Program

2.1. Test Specimens. The designations of the 8 specimens tested are shown in Table 1. Each test specimen was mounted to a pair of columns, as shown in Figure 3. The test setup configuration used in this research is similar with the test scheme conducted by Sudibyo and Chen [15]. The columns and the end-plate connections possessed very high stiffness and strength so that their deformation can be neglected. All the specimens were symmetrical with respect to their center lines and had a clear span length of 1200 mm. The bottom end of each column was connected to a rigid base through a hinge.

Figure 4(a) shows the geometry and dimensions of the cross section used. The cross-sectional steel shape used, which was H 150 × 75 × 5 × 7, had a flange width-to-

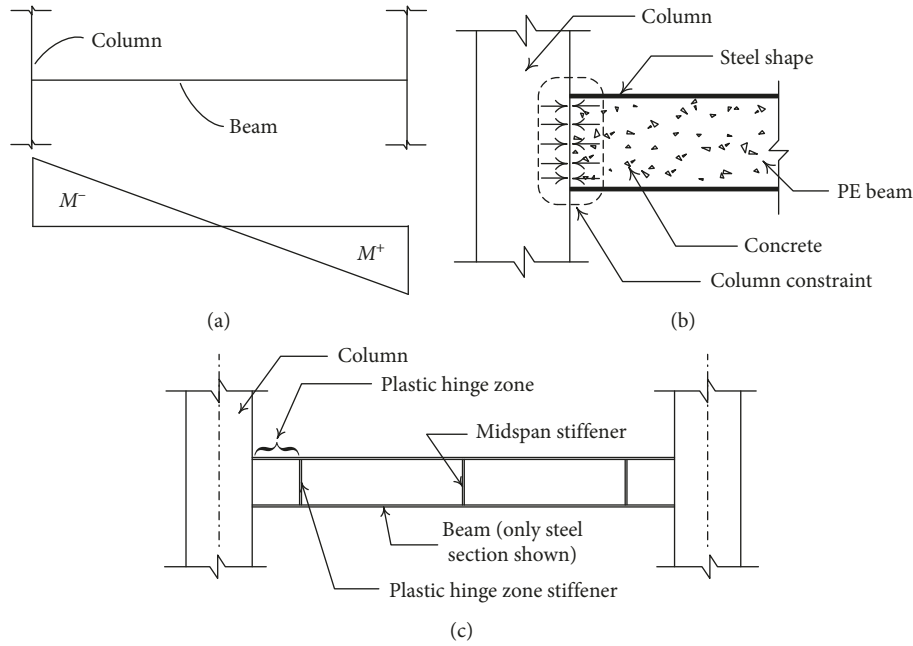


FIGURE 2: PE Beam in a moment resisting frame. (a) Moment distribution of the beam under earthquake type loading. (b) Column constraint at beam end. (c) Plastic hinge zone stiffener and midspan stiffener.

TABLE 1: Details of test specimens.

| Series | Specimen | Steel beam cross section | Connection type ^a | Composite action device ^b |
|--------|----------|--------------------------|------------------------------|--------------------------------------|
| PS | PS-NB | RH 150 × 75 × 5 × 7 | SBC | — |
| | PS-SC | RH 150 × 75 × 5 × 7 | SBC | Shear connector |
| | PS-MS | RH 150 × 75 × 5 × 7 | SBC | Midspan stiffener |
| | PS-HS | RH 150 × 75 × 5 × 7 | SBC | Plastic hinge zone stiffener |
| PW | PW-NB | RH 150 × 75 × 5 × 7 | WBC | — |
| | PW-SC | RH 150 × 75 × 5 × 7 | WBC | Shear connector |
| | PW-MS | RH 150 × 75 × 5 × 7 | WBC | Midspan stiffener |
| | PW-HS | RH 150 × 75 × 5 × 7 | WBC | Plastic hinge zone stiffener |

^aDetails of beam-to-column connection are shown in Figures 5–7. ^bDetails of composite action device are shown in Figure 8.

thickness ratio of 5.4. The ends of cross-sectional steel shapes were connected to the end plates with complete penetration welds. ASTM A36 steel with a nominal yield stress of 250 MPa and concrete with a specified compressive strength of 30 MPa were used to design the specimens.

There were 4 specimens in the PW series. In this group, a type of weakened beam-to-column connections proposed by Chen et al. [11], as shown in Figure 5(a), were used. Theoretically, the geometry of the flange tapering should be determined according to the flexural strength of the whole PE section (i.e., steel shape plus concrete). However, it becomes tedious. Instead, for the purpose of simplicity, the geometry of the flange tapering, as shown in Figure 5(a), was determined based on steel shape alone. Figure 6(a) shows the moment capacity distribution along the beam, where M_{pd} (24.5 kN·m) is the design plastic moment (also the nominal design flexural strength) of H 150 × 75 × 5 × 7 calculated with nominal yield stress of the steel. The plastic moment is calculated as specified in Table 4.1 of ANZI/AISC 360-16 [16]. Projecting the moment capacity of Section C to the beam end resulted in a beam end moment of 0.92 M_{pd} .

When determining the geometry of flange tapering, the beam end moment was controlled in between 0.90 and 0.95 M_{pd} and the distance between the critical section (Section C) and the end of the welding access hole was kept 25 mm.

After the determination of the geometry of the flange tapering, the distribution of nominal design moment capacity M_{nd} , based on whole section, along the beam was calculated and is shown in Figure 6(b). The nominal moment capacity is the moment capacity of the whole composite PE section, with complete composite action, based on the plastic stress distribution method as specified in Section I1.2a of ANZI/AISC 360-16 [16] and schematically explained in Figure 4(b). The factor β_1 used in the calculation is referred to ACI [17]. The M_{nd} (26.9 kN·m) is calculated with nominal yield stress of the steel. The ideal condition for weakened beam-to-column connection is that the sections in the tapered flange region reach their design moment capacity simultaneously [11]. It can be found from Figure 6(b) that the sections between C and D reach their moment capacity almost at the same time. This shows that determining the geometry of the flange tapering based on steel shape alone

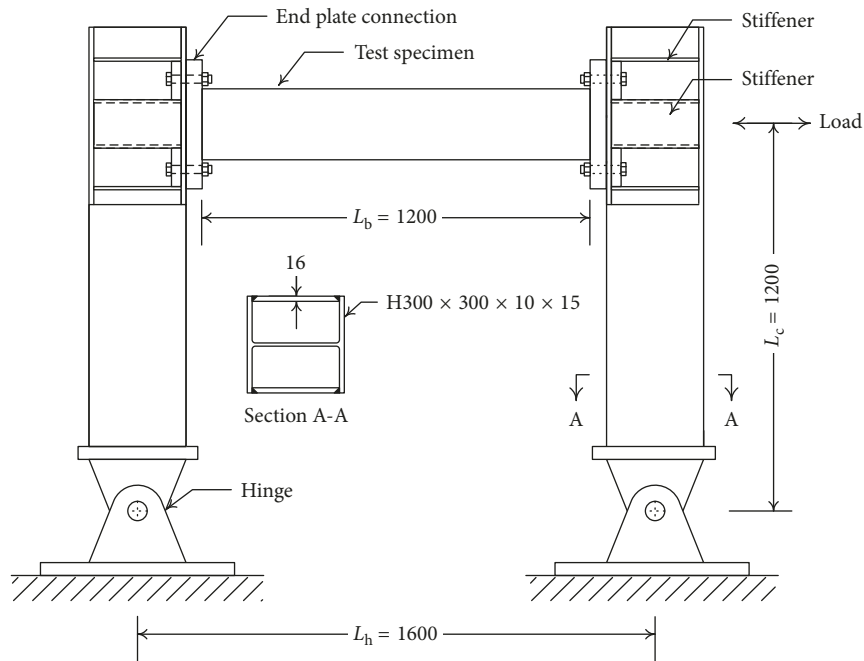


FIGURE 3: The test scheme for beam specimens (unit: mm); adapted from “The Effect of Intermediate Stiffeners on Steel Reinforced Concrete Beam Behaviors” [15].

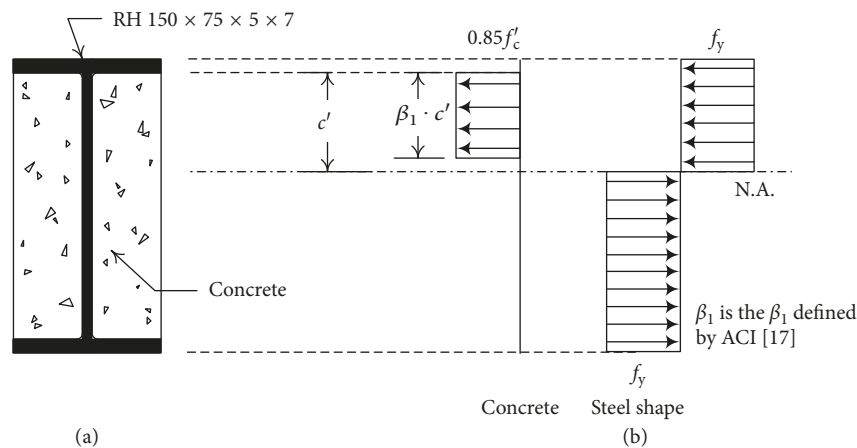


FIGURE 4: (a) Cross section. (b) Plastic stress distribution method, AISC [16].

should be quite satisfactory. The critical section located at Section C. Projecting the design moment capacity of Section C to the beam end resulted in a usable design beam end moment of $0.93M_{nd}$.

There were 4 specimens in the PS series. In this group, strengthened beam-to-column connections, as shown in Figure 5(b), were used. Similar to PW specimens, the cover plates of PS specimens were designed based on steel shape alone for simplicity. The length of the cover plates was determined in such a way that the critical section located at a distance of 25 mm away from the end of the welding access hole. In order to prevent failure at beam end, the moment capacity of the combination of flanges and cover plates was kept at least 1.2 time of M_{pd} . Figure 7(a) shows the design plastic moment distribution along the beam. Figure 7(b)

shows the design nominal moment capacity, based on whole section, along the beam. The critical section located at C and the usable beam end moment was $1.09M_{nd}$. The H shape detail used in this research is the same with the steel configuration conducted by Sudibyo and Chen [15]; therefore, the moment capacity distribution of the steel shape, Figures 6(a) and 7(a), are the same as those in [15].

The specimens with “SC” in their designation were equipped with shear connectors, as shown in Figure 8(a). The specimens with “MS” in their designations had a midspan stiffener installed, as shown in Figure 8(b). The specimens with “HS” in their designations had one plastic hinge zone stiffener installed at each end of the beam. The plastic hinge zone stiffeners were installed at the position 175 mm, which is 1.2 times the beam depth, from the end plate, as shown in

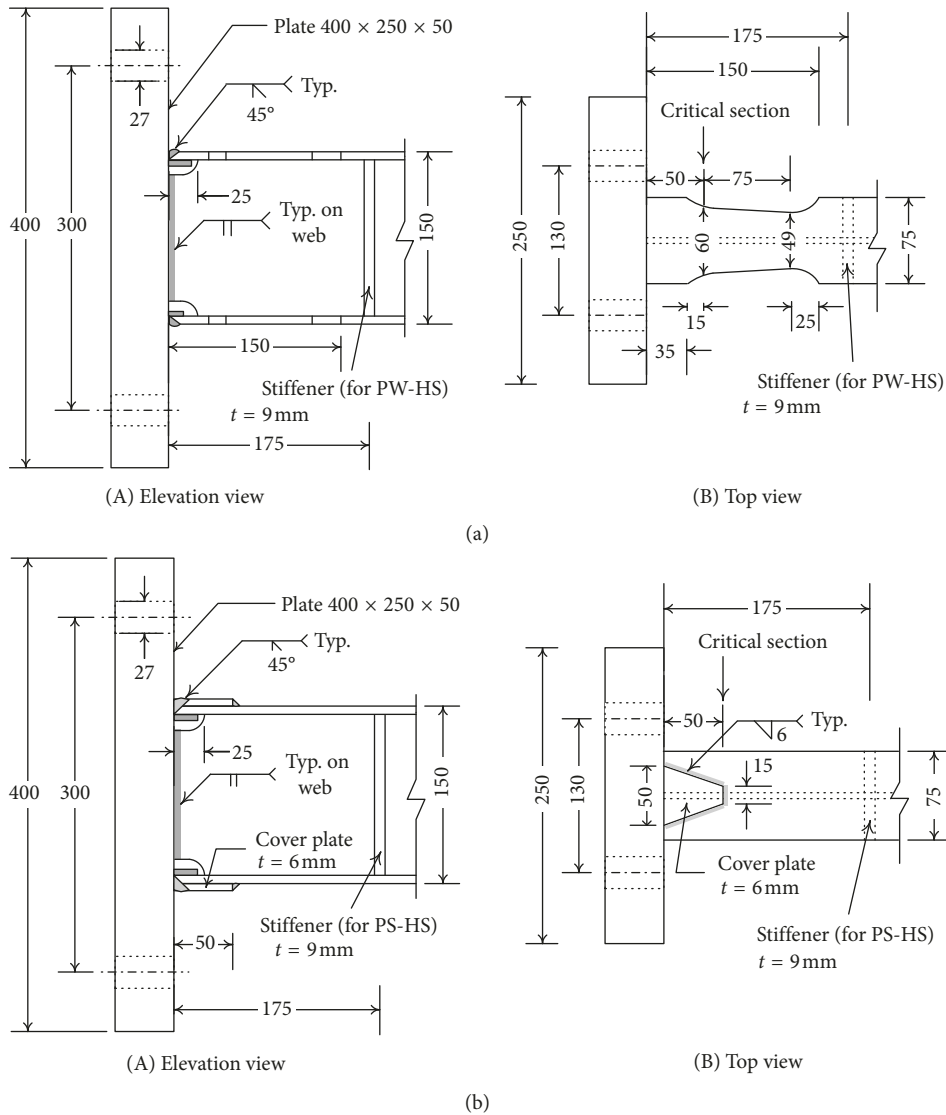


FIGURE 5: Detail of beam-to-column connection for the H shape (unit: mm). (a) WBC connection. (b) SBC connection.

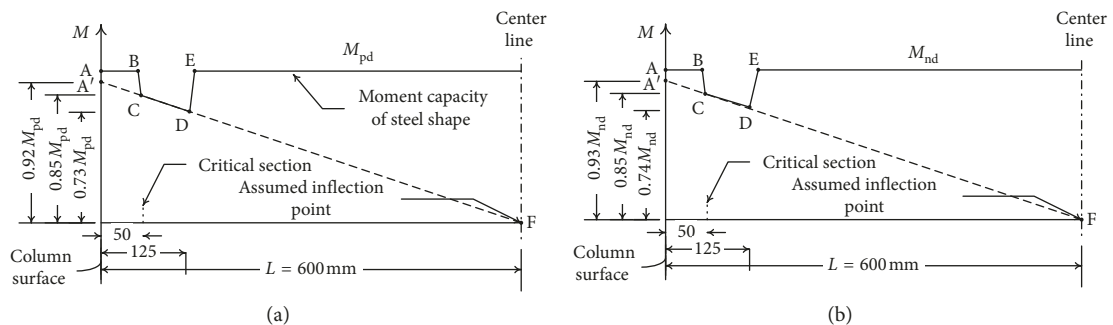


FIGURE 6: Design moment capacity distribution of the beam with WBC connection. (a) Steel shape; adapted from [15]. (b) Whole section.

Figures 5 and 8(b). Specimens with “NB” in their designations used neither shear connector nor stiffener.

The mechanical properties of the H steel shape are listed in Table 2. All the specimens used ready-mixed concrete

without coarse aggregate. The specimens were cast in a horizontal position in two stages: the concrete on one side of the steel beam was cast first, and the concrete on the other side of the steel beam was cast a week later. The compressive

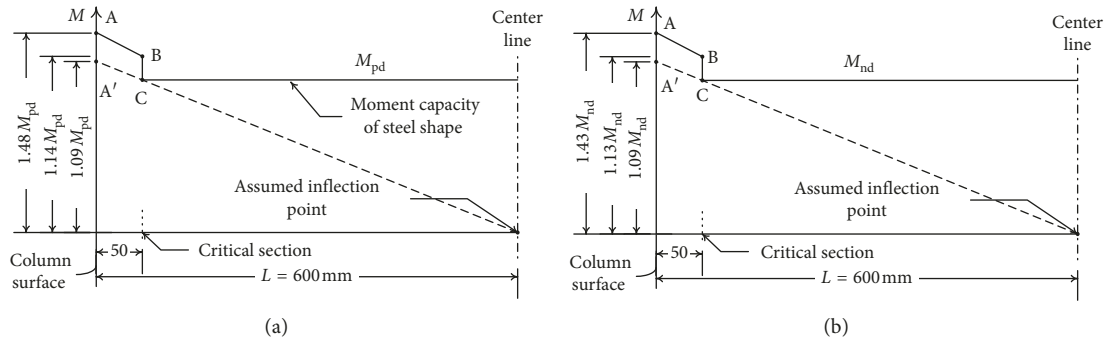


FIGURE 7: Design moment capacity distribution of the beam with SBC connection. (a) Steel shape; adapted from [15]. (b) Whole section.

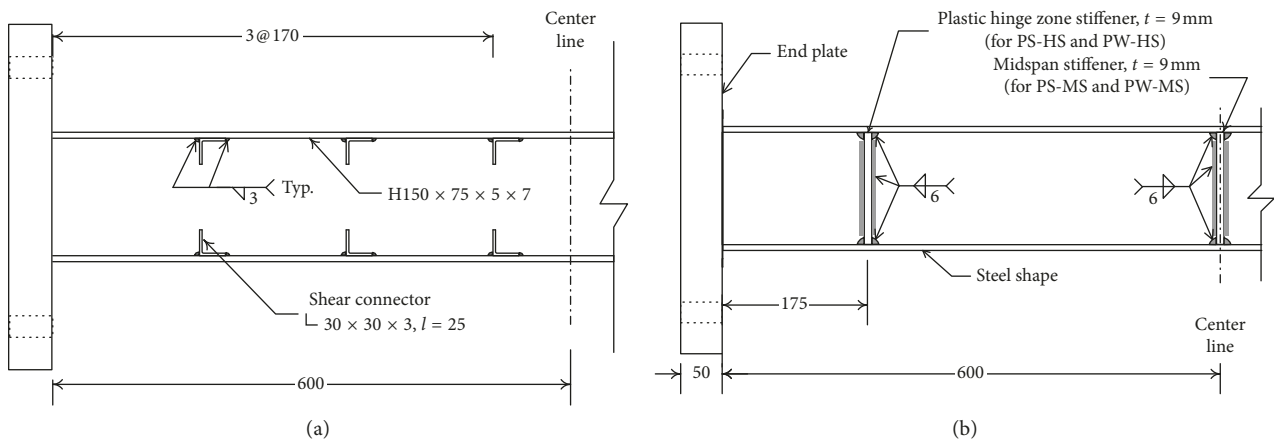


FIGURE 8: Concrete constraint scheme. (a) Elevation view specimens with shear connectors (PS-SC and PW-SC). (b) Elevation view (PS-NB, PS-HS, PS-MS, PW-NB, PW-HS, and PW-MS).

TABLE 2: Mechanical properties of H 150 × 75 × 5 × 7 and concrete.

| Nominal yield stress | Tensile strength of H 150 × 75 × 5 × 7 (MPa) | | | Concrete compressive strength (MPa) | | |
|----------------------|--|--------------------|-------|-------------------------------------|--------|--------|
| | Component | Tensile test f_y | f_u | Nominal strength | Side 1 | Side 2 |
| 250 | Flange | 271.9 | 377.9 | 30 | 39.0 | 37.4 |
| | | 273.7 | 377.1 | | 40.1 | 38.8 |
| | | 271.9 | 371 | | 38.4 | 40 |
| | Average | 272.5 | 375.3 | | 40.9 | 40.2 |
| | Web | 295.7 | 390.2 | | 42.4 | 39.3 |
| | | 290.5 | 392.9 | | 32.8 | 39.6 |
| | | 289.6 | 387.6 | | 37.1 | 38.5 |
| | | Average | 291.9 | | 390.2 | 34.7 |
| | | | | 38.1 | 38.8 | |
| | | | | 38.4 | | |

strength on each side of the steel beam was 38.1 and 38.8 MPa, respectively. The average value (38.4 MPa) was taken as the concrete compressive strength for the specimens.

2.2. Test Setup and Loading Procedure. The test setup is shown in Figure 9. A servo-controlled hydraulic actuator with a capacity of 500 kN was connected to the right column. The actuator was equipped with a built-in load cell and

built-in linear variable differential transducers (LVDT) to measure, respectively, the applied force P and the lateral displacement at the load point. The lateral displacement at the load point is defined as displacement of the right column. The displacement of the left column was measured by an LVDT at the beam center. The average of displacement of the left and right column is defined as the lateral displacement Δ . Rotation gauges R1 and R2 were installed on the end plates of the beam, and rotation gauges R3 and R4 were installed

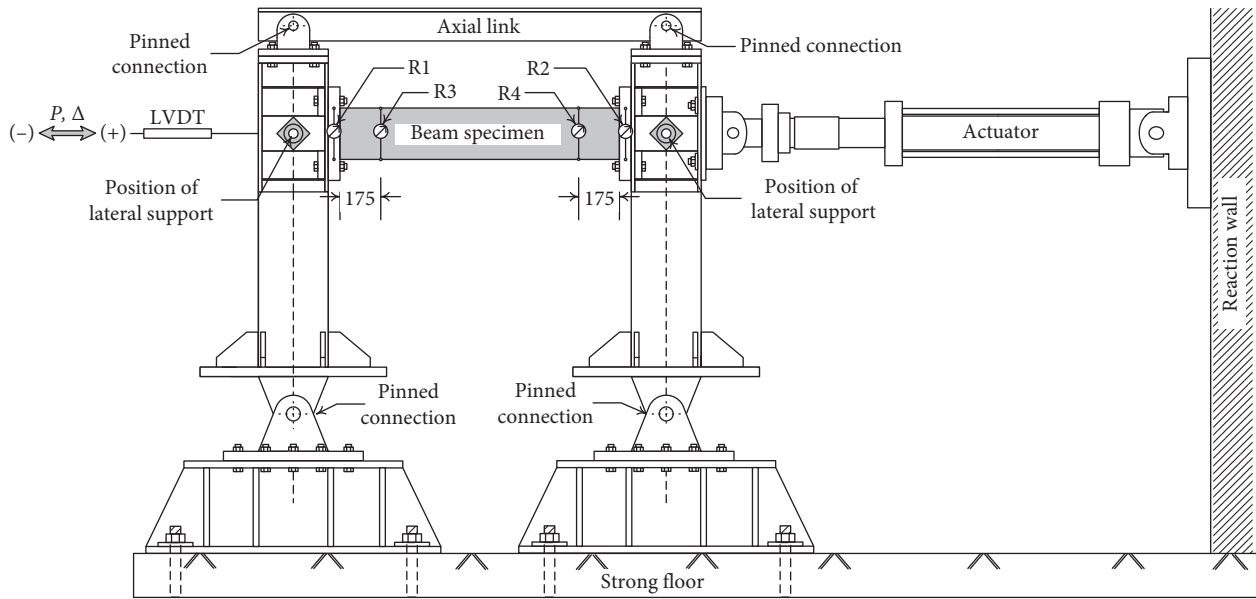


FIGURE 9: Test setup.

175 mm from each beam end. The beam segments between R1 and R3 and between R2 and R4 are defined as plastic hinge zones. The axial link was used to reduce axial force in the specimens.

A quasi-static load was applied under displacement control according to the lateral displacement history shown in Figure 10. Δ_y is defined as the measured lateral displacement of the frame when the moment at beam ends, as indicated in Figure 11, reached nominal moment capacity M_{na} (29.56 kN·m) of the test beams. M_{na} is the moment capacity of the whole composite section, calculated based on the actual material strength, complete composite action, plastic stress distribution method (Section I1. 2a ANZI/AISC 360-16) [16] as shown in Figure 4(b). A Δ_y of 7.5 mm was obtained and used for all the specimens. It is noted that the moment distribution presented in Figure 11 is based on the assumption of antisymmetrical moment distribution of the beam. Since the test scheme (Figure 3) and the H shape configuration (Figure 5) of the specimens used in this research are the same as those used by Sudibyo and Chen [15], the moment distribution of the beam (Figure 11) is the same as that used by Sudibyo and Chen [15]. The load test ended when the strength of the specimen deteriorated more than 20%.

3. Experimental Results and Discussion

3.1. General Behavior. The P versus Δ hysteretic loops for the specimens are shown in Figure 12, and the test results are summarized in Table 3. The drift angle α of the frame is defined as the corresponding Δ divided by L_c . The maximum loads in the positive and negative directions are designated, respectively, as P_{peak}^+ and P_{peak}^- . The maximum load for the tested specimen P_{exp} is defined as the average of P_{peak}^+ and P_{peak}^- . SBC and WBC are intended to prevent failure of the welds connecting the beam and the column, and the failure

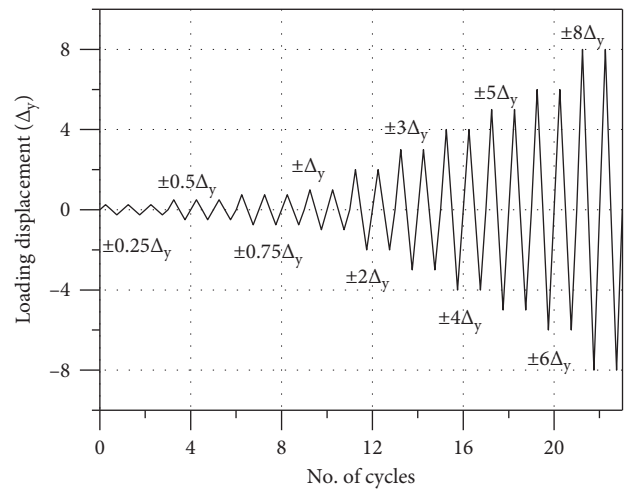


FIGURE 10: Loading history.

of the beam was designed to occur at the critical section of the beam, as shown in Figures 5–7. Therefore, the following analysis is performed based on beam’s moment capacity in the critical section.

According to the moment distribution shown in Figure 11, the moment at the critical section corresponding to P_{exp} , designated as M_{exp} , can be calculated as follows:

$$M_{exp} = \frac{1}{2} P_{exp} L_c \frac{0.5 \cdot L_{cs}}{0.5 L_s} = 0.344 P_{exp} L_c \quad (1)$$

It is worth noting that M_{exp} is an underestimate since the strength of the beam at both ends was, very likely, not developed at the same time. The nominal moment capacities of the critical section $(M_{na})_c$ for PS specimens and PW specimens were 29.6 kN·m and 25.1 kN·m, respectively, as listed in Table 4. The strength ratio γ is defined as the ratio of M_{exp} and $(M_{na})_c$. The plastic moment of the steel shape in

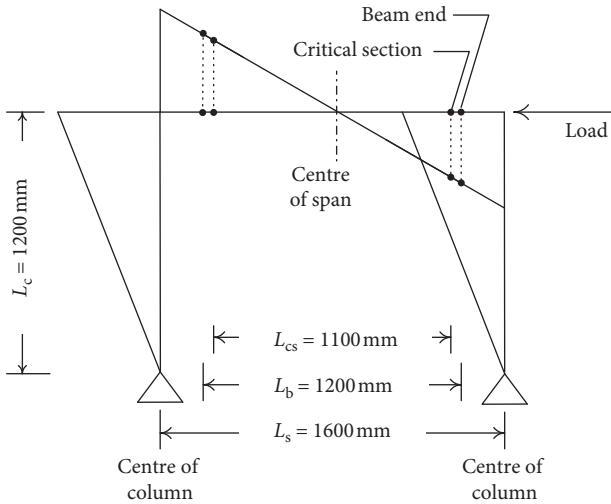


FIGURE 11: Moment distribution of the frame; adapted from “The Effect of Intermediate Stiffeners on Steel Reinforced Concrete Beam Behaviors” [15].

the critical section, calculated using actual yield stress of steel, $(M_p)_c$ for PS specimens and PW specimens were 26.7 kN·m and 22.6 kN·m, respectively, as listed in Table 4. And, the strength ratio γ' is defined as the ratio of M_{exp} and $(M_p)_c$. The strength ratios γ and γ' of all the specimens are listed in Table 3. It is noted that the ratio $(M_{na})_c / (M_p)_c$ was 1.11 for both PS and PW specimens. This indicates that the existence of the concrete raises the moment capacity of the steel beam by about 11%.

The rotation of the left and right plastic hinge zones of the beam are designated as θ_L and θ_R , respectively. θ_L was calculated by subtracting R3 readings from R1 readings, and θ_R was calculated by subtracting R4 readings from R2 readings. Figure 13 shows the lateral load versus plastic hinge rotation hysteresis loops for specimen PS-HS. The P vs. θ skeleton curves based on first cycle of each drift ratio excursion for PS and PW series are shown in Figures 14 and 15, respectively. The yield rotation θ_y and ultimate rotation θ_u were determined based on P vs. θ skeleton curve of each specimen. Figure 16 shows positive P versus θ_L skeleton curve based on the first cycle of each drift angle excursion. The ultimate rotation θ_{ul}^+ is defined as the rotation corresponding to 85% of P_{peak}^+ in the descending portion. The elastic rotation θ_{yl}^+ , as indicated in Figure 16, is the estimated elastic rotation corresponding to P_{peak}^+ . The plastic hinge rotation capacity θ_{pl}^+ was the difference between θ_{ul}^+ and θ_{yl}^+ . Through the procedure aforementioned, θ_{pl}^+ , θ_{pl}^- , θ_{pr}^+ , and θ_{pr}^- for each specimen were determined. The plastic hinge rotation capacity, θ_p , of each specimen is defined as the average of θ_{pl}^+ , θ_{pl}^- , θ_{pr}^+ , and θ_{pr}^- .

3.2. Behaviors of PS Series. The failure procedure for all PS specimens was similar. Concrete crushing and steel flange buckling, as shown in Figure 17(a), was observed when the applied load reached P_{peak}^+ and P_{peak}^- . After that, cracks at the end of the cover plate started to develop and eventually caused the fracture of the steel flange, as shown in

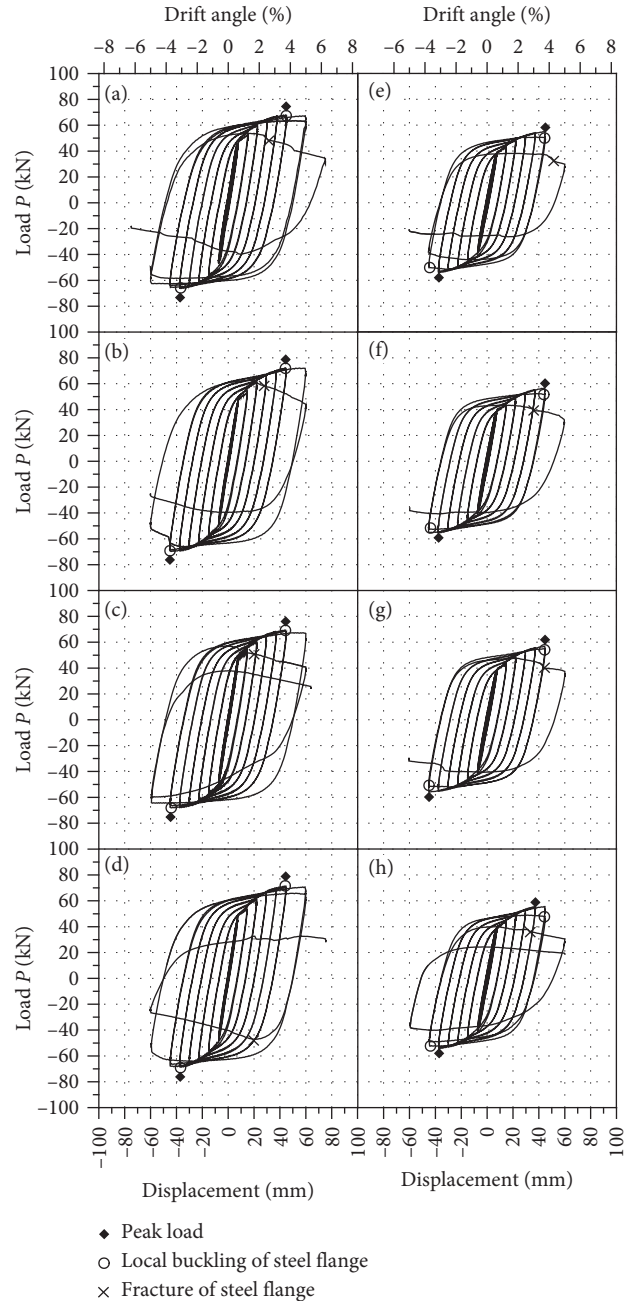


FIGURE 12: Load versus displacement hysteresis loops. (a) PS-NB. (b) PS-SC. (c) PS-MS. (d) PS-HS. (e) PW-NB. (f) PW-SC. (g) PW-MS. (h) PW-HS.

Figure 17(b). The hysteresis loops of the specimens are quite stable up to one or two cycles after local buckling of steel flange occurs.

Figures 18(a)–18(d) show the condition and the crack pattern of PS specimens after the first 5% cycle. The damage on the right end of the specimen is more severe than that on the left end, which indicates that the strength of the beam at the two ends did not develop at the same time. And, P_{exp} and M_{exp} underestimate the real strength of the beams. Consequently, specimen PS-SC, which is considered possessing complete composite action, has a strength ratio γ (0.99) slightly less than 1.0.

TABLE 3: Test result of test specimens.

| Series | Specimen | P_{peak}^+ (kN) | α_{peak}^+ (%) | P_{peak}^- (kN) | α_{peak}^- (%) | P_{exp} (kN) | M_{exp} (kN.m) | γ | γ' | θ_p (%) |
|--------|----------|-------------------|-----------------------|-------------------|-----------------------|----------------|------------------|----------|-----------|----------------|
| PS | PS-NB | 68.0 | 3.75 | -66.3 | -3.13 | 67.2 | 27.70 | 0.94 | 1.04 | 5.44 |
| | PS-SC | 72.3 | 3.75 | -69.8 | -3.75 | 71.1 | 29.31 | 0.99 | 1.10 | 5.21 |
| | PS-MS | 69.5 | 3.75 | -68.2 | -3.75 | 68.8 | 28.39 | 0.96 | 1.06 | 5.67 |
| | PS-HS | 71.4 | 3.75 | -68.8 | -3.13 | 70.1 | 28.91 | 0.98 | 1.08 | 6.11 |
| | Average | | | | | 69.3 | | 0.97 | | 5.61 |
| PW | PW-NB | 54.8 | 3.75 | -54.1 | -3.13 | 54.5 | 22.46 | 0.89 | 0.99 | 4.52 |
| | PW-SC | 56.8 | 3.75 | -55.5 | -3.13 | 56.1 | 23.15 | 0.92 | 1.02 | 4.75 |
| | PW-MS | 56.8 | 3.75 | -55.9 | -3.75 | 56.3 | 23.23 | 0.93 | 1.03 | 4.69 |
| | PW-HS | 55.6 | 3.13 | -54.3 | -3.13 | 55.0 | 22.67 | 0.90 | 1.00 | 4.74 |
| | Average | | | | | 55.5 | | 0.91 | | 4.67 |

TABLE 4: Moment capacity of the section.

| Plastic moment of steel shape (kN.m) | | | | Nominal moment capacity (kN.m) | | | |
|--------------------------------------|-----------------|------|----------------|--------------------------------|------|--------------------|------|
| $M_{pd}^{(a)}$ | $(M_p)_c^{(b)}$ | | $M_{nd}^{(a)}$ | $M_{na}^{(b)}$ | | $(M_{na})_c^{(b)}$ | |
| | PS | PW | | PS | PW | PS | PW |
| 24.5 | 26.7 | 22.6 | 26.9 | 29.6 | 29.6 | 29.6 | 25.1 |

^(a)Calculated with the material's nominal strength. ^(b)Calculated with the material's actual strength (test value).

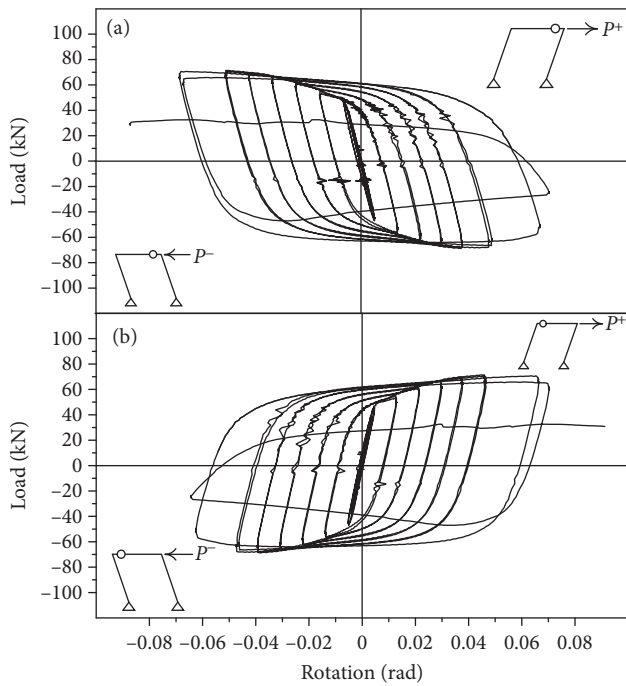


FIGURE 13: Load vs plastic hinge rotation of specimen PS-HS. (a) Right plastic hinge rotation (θ_R). (b) Left plastic hinge rotation (θ_L).

3.3. Behaviors of PW Series. Due to the tapering of the flange, concrete occupied the space where flange was tapered, indicated as “flange concrete” in Figure 19. When the flange concrete was subjected to compressive force, it was pushed sideward and caused concrete damage to occur earlier than that of PS specimens, as shown in Figure 20. Since the flanges of PW specimen were tapered and a smaller width-to-thickness ratio is then resulted, flange local buckling occurred somewhat later than PS specimens did, as indicated in Figure 12.

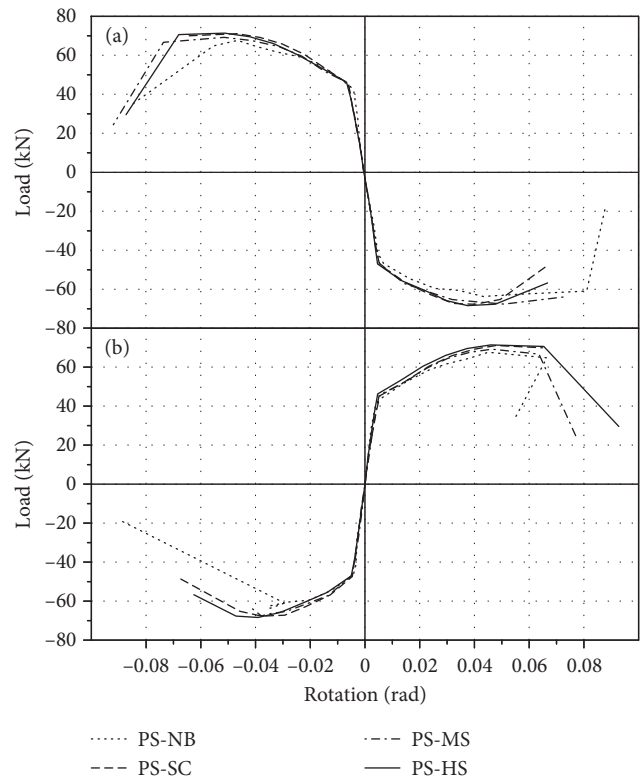


FIGURE 14: Skeleton curve of plastic hinge rotation for PS series. (a) Right plastic hinge rotation (θ_R). (b) Left plastic hinge rotation (θ_L).

The crack patterns of PW specimens, as shown in Figures 18(e)–18(h), also show that the concrete damage on the right end of the specimen is more severe than that on the left end. PW specimens experienced more severe concrete damage than the corresponding PS specimens.

Cracking of the steel flange was observed after peak loads were reached. Cracking, as indicated in Figure 21(a),

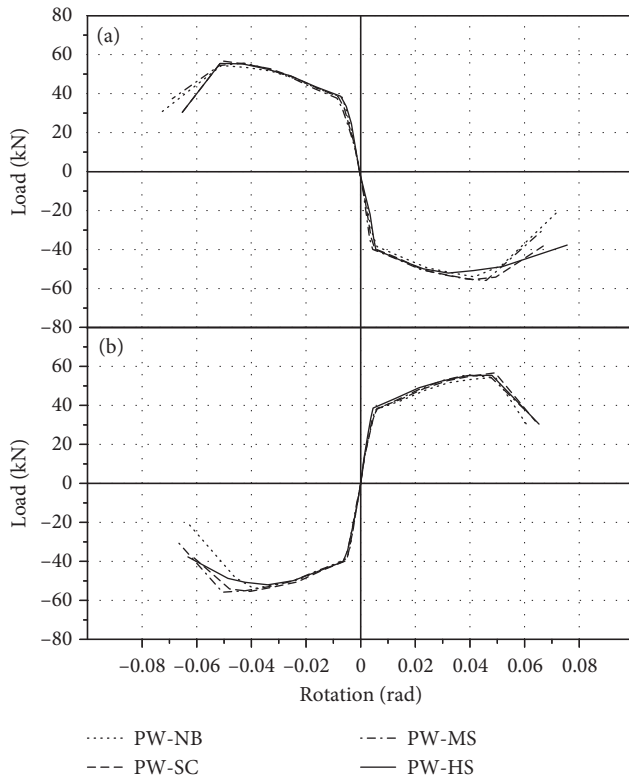


FIGURE 15: Skeleton curve of plastic hinge rotation for PW series. (a) Right plastic hinge rotation (θ_R). (b) Left plastic hinge rotation (θ_L).

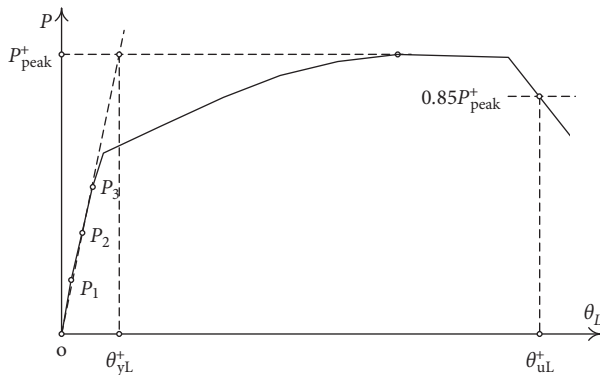


FIGURE 16: The definition of θ_u and θ_y .

started from the center of the flange just above the end of the welding access hole. The crack then extended toward the tapered region of the flange. Figure 21(b) shows the flange fracture of PW-NB specimen. The premature flange fracture and the extra concrete damage near the flange tapering region reduced the experimental strength of the specimens. As a result, the strength ratio of PW-SC (0.92) is even lower than that of PS-SC (0.99) by about 7%.

The premature flange fracture should be deferred, and higher flexural strength and ductility should be developed if larger access hole-taper start clearance is provided [11].

3.4. Effectiveness of Intermediate Stiffeners. Since premature failure of the PW specimens was observed, it is more reliable to compare the effectiveness of composite action based on test results from PS specimens. Take PS-SC as a reference, the $P_{exp}/(P_{exp})_{SC}$ ratio and $\theta_p/(\theta_p)_{SC}$ ratio of PS-NB, PS-MS, and PS-HS are calculated and listed in Table 5, where $(P_{exp})_{SC}$ and $(\theta_p)_{SC}$ are the P_{exp} and θ_p of PS-SC specimen.

The $P_{exp}/(P_{exp})_{SC}$ ratio for PS-NB (0.94) is apparently lower than 1.0. This indicates that column constraint alone is not quite enough to develop full composite action of the PE beam regardless of the fact that plastic hinge rotation capacity of PS-NB is no less than that of PS-SC.

The $P_{exp}/(P_{exp})_{SC}$ and $\theta_p/(\theta_p)_{SC}$ ratios of PS-MS are 0.97 and 1.09, respectively. They are higher than those for PS-NB specimen. This indicates that the midspan stiffener is able to provide extra constraint and develop higher degree of composite action of the PE beam. However, the effectiveness may diminish for longer beams.

The $P_{exp}/(P_{exp})_{SC}$ for PS-HS is 0.99 which is in the range of experimental error. In addition, the $\theta_p/(\theta_p)_{SC}$ is as high as 1.17. Test data indicate that the plastic hinge zone stiffener is able to develop a very high degree of composite action and to enhance significantly the ductility of the PE beams. Usually, the length of the plastic hinge zone is in the range of 1.0 to 1.5 times the beam depth, no matter how long the beam is. Therefore, the position of the end stiffener does not vary so much, and the effectiveness of the plastic hinge zone stiffener will not diminish as the beam length becomes larger. Test results indicated that the plastic hinge zone stiffener used in this study has the potential to replace shear connectors on developing the beam composite action. With the existence of plastic hinge zone stiffener in the PE beam, less shear connectors or shear studs are required to hold the concrete encasement between the beam's webs; therefore it will simplify the fabrication of PE beam.

3.5. Strengthened and Weakened Steel Beam-to-Column Connection. The θ_p that PS specimens achieved ranges from 5.21 to 6.11% which is much greater than 4%. This is considered sufficient for seismic design of highly ductile members as required by AISC seismic provision [18]. For PW specimens, although premature failure occurred, the θ_p achieved (4.52 to 4.75%) is also sufficient for beams in highly seismic zones. Test results shows that the application of SBC and WBC on the PE beams worked satisfactorily. In addition, designing SBC and WBC based on moment capacity of the H steel shape instead of the whole section seems to have worked well for the specimens tested in this study.

The average P_{exp} of PS specimens (69.3 kN) is 25% higher than that of PW specimens (55.5 kN). This phenomenon can be attributed to three factors. The first factor comes from the beam-to-column connection scheme itself. The usable design beam end moment for SBC is $1.09 M_n$, which is 17% higher than that of WBC ($0.93 M_n$). The influence of this factor will be reduced as the moment gradient of the beam becomes smaller. The second factor is the premature failure of the flange. And, the third factor is the concrete damage next to the tapered flange.



FIGURE 17: Damage of selected PS specimens. (a) Local buckling of the steel. (b) Fracture of the steel flange of specimen PS-NB.

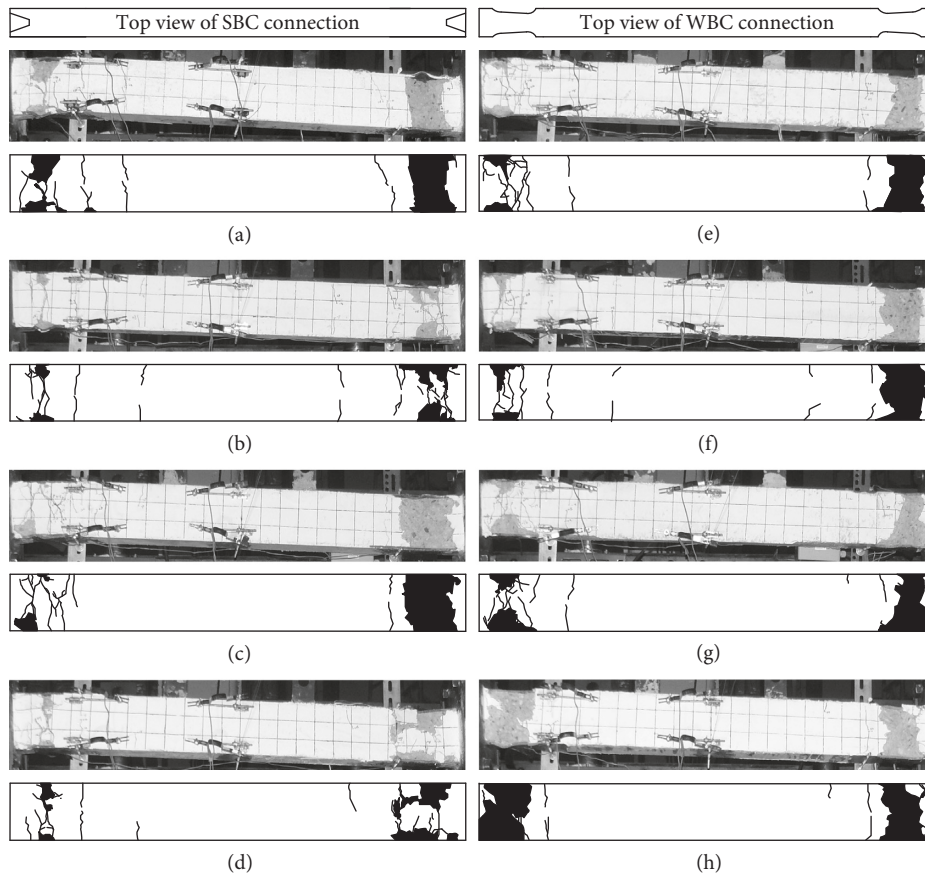


FIGURE 18: Condition and crack pattern of all specimens at 1st 5% drift angle cycle. (a) PS-NB. (b) PS-SC. (c) PS-MS. (d) PS-HS. (e) PW-NB. (f) PW-SC. (g) PW-MS. (h) PW-HS.

The averaged θ_p value of PS specimens is 20% higher than that of PW specimens. The premature fracture of the flange and the damage of the concrete next to the tapered flange make major contributions to this phenomenon. Providing sufficient “access hole-taper start clearance,” as shown in Figure 22, should be able to avoid premature failure of the flange.

For the PW specimens tested here, a “flange net width w_n ” can be estimated according to the fracture path observed, as shown in Figure 23, and Section B4.3b of AISC specification [16], as follows:

$$w_n = 67 + 2 \times \frac{15^2}{4 \times 18.5} = 73 \text{ (mm)}. \quad (2)$$

The calculated w_n equals to 73 mm which is smaller than the flange gross width (75 mm). This provides an explanation for the premature failure of the flange. It is suggested that, to prevent the premature failure of WBC, an access hole-taper start clearance that ensures a net flange width w_n greater than flange gross width should be provided.

The concrete damage next to the tapered flange should can be mitigated by removing the concrete in the tapered

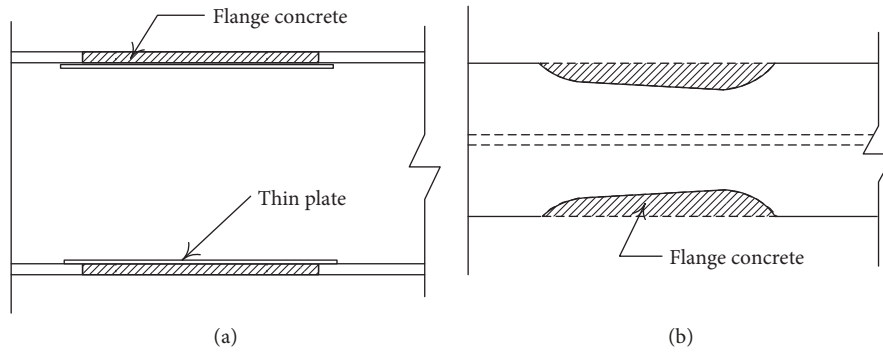


FIGURE 19: Flange concrete of PW specimens. (a) Side view. (b) Top view.

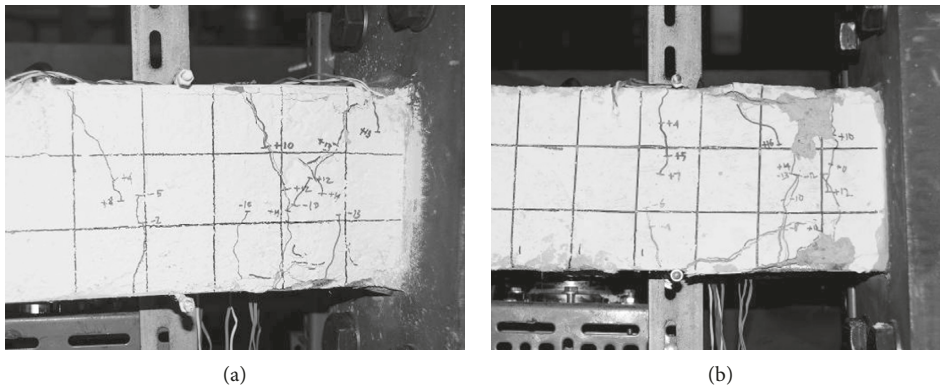


FIGURE 20: Crack pattern of PS-NB and PW-NB at 2nd 2.5% drift angle cycle. (a) PS-NB. (b) PW-NB.

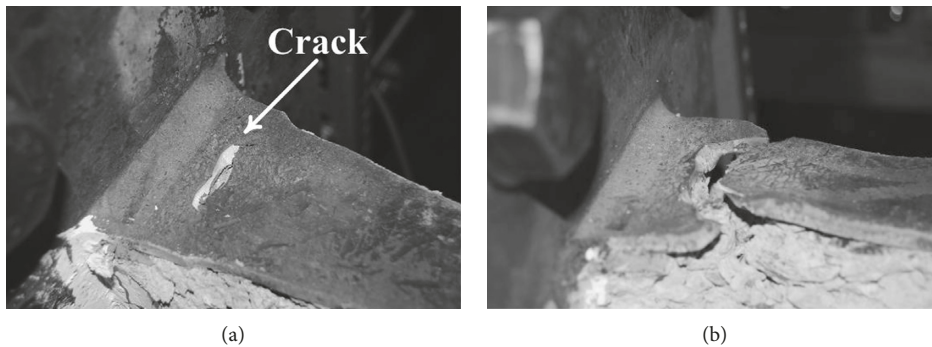


FIGURE 21: Flange crack and fracture of specimen PW-NB. (a) Beginning of steel flange fracture. (b) Fracture of the steel flange.

TABLE 5: The effectiveness of concrete constraint schemes.

| Specimen | PS-NB | PS-MS | PS-HS |
|----------------------------|-------|-------|-------|
| $P_{exp}/(P_{exp})_{SC}$ | 0.94 | 0.97 | 0.99 |
| $\theta_p/(\theta_p)_{SC}$ | 1.04 | 1.09 | 1.17 |

flange area (termed as flange concrete herein), as the shaded region indicated in Figure 19. This can be accomplished by installing thin steel plates in the area of tapered flange before concrete is casted, as indicated in Figure 19(a).

Thick plate welding is considered to have adverse effect on ductility development of strengthened beam-to-column connections. Since the PS specimens tested here

were small-scale specimens, the thick plate welding effect did not show here. However, in the real structure, the thick plate welding effect is likely to emerge, and the ductility of the strengthened connection may be reduced.

4. Conclusions

Eight partially concrete encased steel (PE) beams were fabricated and tested under earthquake type loading. The effectiveness of midspan stiffeners and plastic hinge zone stiffeners in enhancing composite action and ductility of the PE beams was studied. The strength and ductility of strengthened beam-to-column connection and weakened

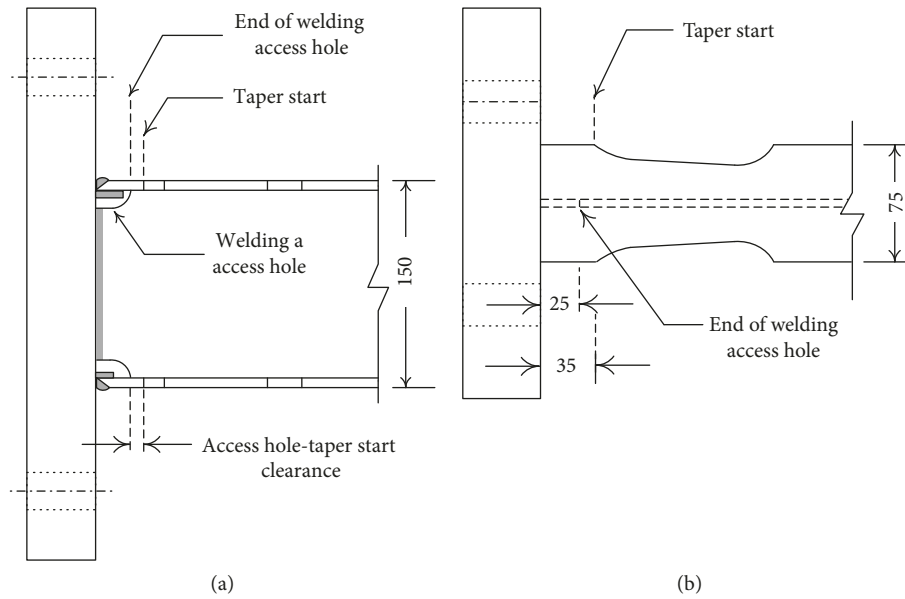


FIGURE 22: Access hole-taper start clearance of WBC. (a) Elevation view. (b) Top view.

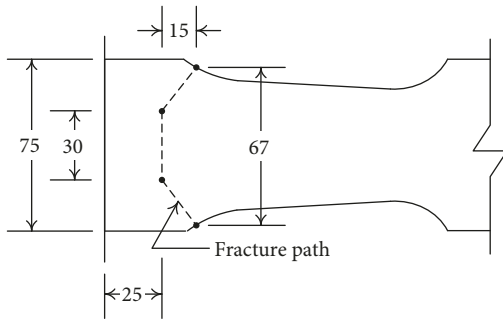


FIGURE 23: Observed flange fracture path of specimen PW-NB (unit: mm).

beam-to-column connection were also investigated. Based on the experimental results reported herein, the following conclusions can be drawn:

- (1) The plastic hinge zone stiffener used in this study can successfully develop the composite action of PE beams. The flexural strength of the beam can be fully developed and the ductility of the beam was 17% higher than that of beams with shear connectors. The plastic hinge zone stiffener has the potential of replacing shear connectors for developing composite action of the beam.
- (2) The midspan stiffener used in this study provides certain effect on developing composite action of PE beams. However, the composite action developed was less complete as the beams use shear connectors.
- (3) The strengthened and weakened beam-to-column connections, which were used to enhance the ductility of steel beams, can also be implemented in PE beams. The ductility of the specimens tested is

high enough to be used in buildings in highly seismic zones.

- (4) Design of strengthened and weakened beam-to-column connection based on the cross-sectional steel shape alone, instead of the whole section, was able to lead to high ductility of the beams. This can greatly simplify the design of strengthened and weakened beam-to-column connections of PE beams.
- (5) Premature flange fracture may happen if the access hole-taper start clearance is not long enough. It is suggested that an access hole-taper start clearance that ensures a net flange width greater than flange gross width should be provided.
- (6) For beams with weakened beam-to-column connections, the concrete near the tapered flange region was subjected to stress concentration and suffered more severe damage. This brings more concrete cracks, lower flexural strength, and low flexural ductility to the beams. This phenomenon can be mitigated by removing the concrete next to the flange at the flange level.

Symbols

- c' : Distance from the top of concrete to the neutral axis of the composite section
- f_y : Yield stress of steel
- f_u : Ultimate stress of steel
- L_b : Length of the beam (refer Figure 11)
- L_c : Length between the column's pinned connection to the beam center (refer Figure 11)
- L_{cs} : Distance between the two critical section (refer Figure 11)
- L_s : Distance between the columns (refer Figure 11)

| | |
|---------------------|---|
| M_{exp} : | Moment at the critical section corresponding to P_{exp} |
| M_{na} : | Nominal moment capacity is the moment capacity of whole composite section, based on actual material strength |
| $(M_{na})_c$: | Nominal moment capacity of critical section |
| M_{nd} : | Design nominal flexural strength of the whole section (composite section), based on nominal material strength |
| M_{pd} : | Design plastic moment of the steel shape, based on nominal material strength |
| $(M_p)_c$: | Plastic moment of the steel shape at critical section, based on actual material strength |
| P : | Applied force |
| P_{peak}^+ : | Maximum load in the positive direction |
| P_{peak}^- : | Maximum load in the negative direction |
| P_{exp} : | Average of P_{peak}^+ and P_{peak}^- |
| $(P_{exp})_{SC}$: | P_{exp} of PS-SC specimen |
| ω_n : | Flange net width |
| α : | Drift angle |
| α_{peak}^+ : | Drift angle when reaching the maximum load in the positive direction |
| α_{peak}^- : | Drift angle when reaching the maximum load in the negative direction |
| β_1 : | Coefficient for determining concrete stress block height, based on ACI [16]. |
| γ : | Strength ratio $M_{exp}/(M_{na})_c$ |
| γ' : | Strength ratio $M_{exp}/(M_p)_c$ |
| θ_L : | Rotation of the left plastic hinge zones |
| θ_p : | Plastic rotation |
| $(\theta_p)_{SC}$: | θ_p of PS-SC specimen |
| θ_{pL}^+ : | Plastic rotation of left plastic hinge zone in positive loading direction |
| θ_{pL}^- : | Plastic rotation of left plastic hinge zone in negative loading direction |
| θ_{pR}^+ : | Plastic rotation of right plastic hinge zone in positive loading direction |
| θ_{pR}^- : | Plastic rotation of right plastic hinge zone in negative loading direction |
| θ_R : | Rotation of the right plastic hinge zones |
| θ_u : | Ultimate rotation |
| θ_{uL}^+ : | Ultimate rotation of left plastic hinge zone in positive loading direction |
| θ_{yL}^+ : | Yield rotation of left plastic hinge zone in positive loading direction |
| θ_y : | Yield rotation |
| Δ : | Lateral displacement |
| Δ_y : | Measured lateral displacement of the frame when the moment at beam ends reached M_{na} . |

Data Availability

The data used to support the findings of this study are available from the corresponding author upon request.

Conflicts of Interest

The authors declare that there are no conflicts of interest regarding the publication of this paper.

References

- [1] C. C. Chen, T. Sudibyo, and Erwin, "Behavior of partially concrete encased steel beam under cyclic loading," *International Journal of Steel Structures*, pp. 1–14, 2018.
- [2] A. Kodaira, H. Fujinaka, H. Ohashi, and T. Nishimura, "Fire resistance of composite beams composed of rolled steel profile concreted between flanges," *Fire Science and Technology*, vol. 23, no. 3, pp. 192–208, 2004.
- [3] P. A. G. Piloto, A. B. R. Gavilan, L. M. R. Mesquita, and C. Goncalves, "High temperature tests on partially encased beams," in *Proceedings of 7th International Conference on Structure in Fire*, Zurich, Switzerland, June 2012.
- [4] P. A. G. Piloto, A. B. R. Gavilan, M. Zipponi, A. Marini, L. M. R. Mesquita, and G. Plizzari, "Experimental investigation of the fire resistance of partially encased beams," *Journal of Constructional Steel Research*, vol. 80, pp. 121–137, 2013.
- [5] R. Kindmann, R. Bergmann, L. G. Cajot, and J. B. Schleich, "Effect of reinforced concrete between the flanges of the steel profile of partially encased composite beams," *Journal of Constructional Steel Research*, vol. 27, no. 1–3, pp. 107–122, 1993.
- [6] S. D. Nardin and A. L. H. C. Debs, "Study of partially encased steel composite beams with innovative position of stud bolts," *Journal of Constructional Steel Research*, vol. 65, no. 2, pp. 342–350, 2009.
- [7] J. Hegger and C. Goralski, "Structural behavior of partially concrete encased composite sections with high strength concrete," in *Proceedings of 5th International Conference in Composite Construction in Steel and Concrete*, pp. 346–355, Mpumalanga, South Africa, July 2004.
- [8] Y. Chen, W. Li, and C. Fang, "Performance of partially encased composite beams under static and cyclic bending," *Structures*, vol. 9, pp. 29–40, 2017.
- [9] J. Lindner and N. Budassis, "Lateral torsional buckling of partially encased composite beams without concrete slab," in *Proceedings of Composite Construction in Steel and Concrete IV Conference*, pp. 117–128, The United Engineering Foundation ASCE, Banff, AB, Canada, May–June 2000.
- [10] A. Plumier, "Behavior of connections," *Journal of Constructional Steel Research*, vol. 29, no. 1–3, pp. 95–119, 1994.
- [11] S. J. Chen, C. H. Yeh, and J. M. Chu, "Ductile steel beam-to-column connection for seismic resistance," *Journal of Structural Engineering*, vol. 122, no. 11, pp. 1292–1299, 1996.
- [12] S. J. Chen, J. M. Chu, and Z. L. Chou, "Dynamic behavior of steel frames with beam flanges shaved around connection," *Journal of Constructional Steel Research*, vol. 42, no. 1, pp. 49–70, 1997.
- [13] T. Kim, A. S. Whittaker, A. S. J. Gilani, V. V. Bertero, and S. M. Takhirov, "Cover-plate and flange-plate steel moment-resisting connections," *Journal of Structural Engineering*, vol. 128, no. 4, pp. 474–482, 2002.
- [14] E. A. Sumner and T. M. Murray, "Behavior of extended end-plate moment connections subject to cyclic loading," *Journal of Structural Engineering*, vol. 128, no. 4, pp. 501–508, 2002.
- [15] T. Sudibyo and C. C. Chen, "The effect of intermediate stiffeners on steel reinforced concrete beam behavior," *World Academy of Science, Engineering and Technology, International Journal of Civil and Environmental Engineering*, vol. 6, no. 8, 2012.

- [16] ANSI/AISC 360-16, *Specification for Structural Steel Buildings*, American Institute of Steel Construction, Chicago, IL, USA, 2016.
- [17] ACI, *Building Code Requirement for Structural Concrete ACI 318-99*, American Concrete Institute, Farmington Hills, MI, USA, 2014.
- [18] ANSI/AISC 341-16, *Seismic Provision for Structural Steel Buildings*, American Institute of Steel Construction, Chicago, IL, USA, 2016.



Hindawi

Submit your manuscripts at
www.hindawi.com

